

Hamiltonian Monte Carlo reconstruction from peculiar velocities

Aurélien Valade,^{1,2} Yehuda Hoffman,³ Noam I Libeskind,^{1,2} and Romain Graziani,⁴

¹Leibniz-Institut für Astrophysik Potsdam (AIP), An der Sternwarte 16, 14482 Potsdam, Germany

²Univ Lyon, Univ Claude Bernard Lyon 1, CNRS, IP2I Lyon / IN2P3, IMR 5822, F-69622, Villeurbanne, France

³Racah Institute of Physics, Hebrew University, Jerusalem 91904, Israel

⁴OSE Engineering, 1 route de Versailles, 78470 Saint-Remy-Les-Chevreuses, France

Accepted XXX. Received YYY; in original form ZZZ

ABSTRACT

The problem of the reconstruction of the large scale density and velocity fields from peculiar velocities surveys is addressed here within a Bayesian framework by means of Hamiltonian Monte Carlo (HMC) sampling. The HAMILTONIAN Monte Carlo reconstruction of the Local Environment (HAMLET) algorithm is designed to reconstruct the linear large scale density and velocity fields in conjunction with the undoing of lognormal bias in the derived distances and velocities of peculiar velocities surveys such as the Cosmicflows data. The HAMLET code has been tested against Cosmicflows mock catalogs consisting of up to 3×10^4 data points with mock errors akin to those of the Cosmicflows-3 data, within the framework of the Λ CDM standard model of cosmology.

The HAMLET code outperforms previous applications of Gibbs sampling MCMC reconstruction from the Cosmicflows-3 data by two to four orders of magnitude in CPU time. The gain in performance is due to the inherent higher efficiency of the HMC algorithm and due to parallel computing on GPUs rather than CPUs. This gain will enable an increase in the reconstruction of the large scale structure from the upcoming Cosmicflows-4 data and the setting of constrained initial conditions for cosmological high resolution simulations.

Key words: Cosmology – Large-scale structure of Universe – dark matter – methods: data analysis

1 INTRODUCTION

The large scale structure (LSS) of the Universe, as manifested by the large scale density and velocity fields of galaxies and of the underlying dark matter (DM), reflects the primordial state of the Universe and serves as a probe of the cosmological parameters that define the standard model of cosmology (Peebles 1980; Weinberg 2008). In the standard cosmological model the density and velocity fields are strongly related by the continuity equation and in principle knowledge of one determines the other, in particular in the linear regime. Galaxies are the most common tracers of the LSS and are used to uncover, or reconstruct, the large scale density and velocity fields. Yet, galaxies are biased tracers of the underlying density field (Dekel & Silk 1986). Their radial peculiar velocities (namely the residual velocity when the Hubble expected expansion is subtracted from the total velocity) are induced by the density deviations from a homogeneous and isotropic universe. It follows that the velocity field derived from the velocities of galaxies can be used to uncover the underlying matter, and in particular the DM, distribution and thereby shed light on the so-called galaxy bias.

The recognition that at low redshifts, $z \lesssim 0.1$, peculiar velocities are practically the only unbiased tracer of the full density field motivated large scale surveys of galaxy peculiar velocities

starting with Aaronson et al. (1982), followed by the Seven Samurai discovery of the Great Attractor (Lynden-Bell et al. 1988) and more recently the three data releases of the Cosmicflows project (Tully et al. 2008, 2013, 2016, CF1, CF2 and CF3, respectively). The availability of peculiar velocity surveys prompted the efforts to reconstruct the continuous density and three dimensional (3D) velocity fields spanned on a regular grid (e.g. Bertschinger & Dekel 1989; Zaroubi et al. 1999; Hoffman et al. 2018; Lavaux 2016). The reconstruction of the LSS from peculiar velocity surveys is challenging - the data is sparse, non-uniform, anisotropic, extremely noisy and biased. Yet, the highly correlated nature of the velocity field, predicted by the standard model, acts to counter balance these hurdles and makes the reconstruction of the LSS possible.

The radial peculiar velocity of a galaxy is not a directly observed quantity but is an inferred one. (Throughout the paper the term ‘velocity’ stands for the radial peculiar velocity.) In fact surveys of galaxy velocities are actually surveys of galaxy distances and redshifts, from which velocities are inferred. Yet, galaxy distances are inferred from the observed distance moduli. The normally distributed observational uncertainties of the distance moduli are transformed into lognormal errors and thereby to a bias in the estimated distances and velocities of galaxies. This lognormal bias is traditionally associated with the Malmquist bias that severely af-

fects the analysis of galaxy velocities surveys (Strauss & Willick 1995; Hoffman et al. 2021). The relative distance errors in the Cosmicflows database are predominantly of the order of $\sim 20\%$, which translate to velocity errors of that order of the Hubble velocity. For a galaxy at a distance of $100 h^{-1}\text{Mpc}$ say (where h is Hubble's constant expressed in units of 100 km/s/Mpc) the typical uncertainty on the velocity is 2000 km/s . In the ΛCDM standard model of cosmology with the Planck parameters (Ade et al. 2016) the predicted scatter of field galaxies is $\sim 350 \text{ km/s}$. This sets the stage for the enormous challenge one faces in attempting to recover the full density and velocity fields from velocities surveys - from sparse, nonuniform, anisotropic and biased data with a typical noise over signal ratio as small as $\sim 15\%$. Another obstacle to overcome is that only the radial component of the velocity is estimated yet a reconstruction of the 3D velocity vector field is needed.

It is clear that the data itself cannot determine the density and velocity fields even within the data zone, namely the regions of space that are sampled by the data, let alone outside it. Something else, beyond the data, is needed in order to infer from the radial component of the velocity their three Cartesian components and the associated density field. This was done first by POTENT algorithm (Bertschinger & Dekel 1989), which assumed the linear theory of gravitational instability in an expanding universe. Yet no assumption was made by POTENT on the statistical nor on the random nature of the underlying density and velocity field.

One of the basic tenets of the ΛCDM model is that the primordial perturbation field constitutes a random Gaussian field, and as such its properties are determined by its power spectrum. Furthermore, in its linear regime the density and velocity fields are linearly related and the knowledge of one determines the other. This has led to a Bayesian approach to the reconstruction of the LSS that relies explicitly on the Gaussianity of the density and/or velocity fields by means of the Wiener filter (WF) and constrained realizations (CRs) of Gaussian random fields (Hoffman & Ribak 1991; Zaroubi et al. 1995, 1999; Sorce et al. 2016; Hoffman et al. 2021). A later development has been made by employing by means Markov Chains Monte Carlo (MCMC) sampling (Lavaux 2016; Graziani et al. 2019).

In both approaches, the WF/CRs and the MCMC, the estimation of the desired density and velocity fields proceeds by the estimation of their posterior probability distribution functions (PDFs) given the data and the assumed ΛCDM model. Yet, the two methods treat uncertainties that lie outside the formalism of Gaussian random fields in radically different ways. This is most strongly manifested by the way the lognormal bias is treated. In the WF/CRs approach the correction of the lognormal bias is done outside and independently of the WF/CRs analysis. Namely a procedure is applied to correct the bias, yielding bias corrected estimated distances and velocities of the data points, and then the WF/CRs machinery is applied to the correct data (Sorce 2015 and independently in Hoffman et al. 2021). Such an approach enables the linear reconstruction from the biased-corrected data by means of an exact analytical solutions. The MCMC adopts a holistic nature to the problem and combines all the uncertainties of the data into one PDF. In particular, statistical assumptions are made on the distribution of the distances of the data points and on the errors of the observed distance moduli. Such an approach defies an exact analytical solutions and the estimation is done by means of MCMC sampling. Gibbs sampling is used by Lavaux (2016) and by Graziani et al. (2019).

The aim of the present paper is to present a new numerical approach to the MCMC algorithm of Lavaux (2016) and by Graziani et al. (2019). The Gibbs sampling algorithm suffers from a slow convergence and is very CPU inefficient in comparison with the

WF/CRs formalism. A very considerable improvement is presented here by a numerical implementation of the Hamiltonian Monte Carlo (HMC) sampling technique. The HMC sampling technique was applied before to reconstruct the LSS from a galaxy redshifts survey by Jasche & Lavaux (2019) and it is applied here for the first time to a galaxy velocities survey. Both the Gibbs sampling based MCMC reconstruction implementations and the present HMC one are constructed within the same theoretical framework and to the extent that they are applied to the same data aiming at the same resolution they should yield very similar results. Our motivation here is to considerably improve the numerical efficiency of MCMC algorithm, aiming in particular to achieve the numerical resolution needed for setting up constrained initial conditions for numerical simulations of the local universe (e.g. Yepes et al. 2014; Sorce et al. 2016; Libeskind et al. 2020). The HAMILTONIAN Monte Carlo reconstruction of the Local Environment (HAMILLET) code is presented here and is tested against a mock catalog. The comparison of the application of the HAMILLET code and a WF/CRs reconstruction is presented in Valade, Hoffman and Libeskind (in prep).

The paper starts with a detailed description of the HMC methods (Section 3). A description of the application of the HAMILLET code to a mock velocity survey and its analysis follows (Section 5). A summary and discussion section concludes the paper (Section 6).

2 BAYESIAN INFERENCE OF THE LARGE SCALE STRUCTURE

The Bayesian probabilistic approach is adopted here, according to which the PDF represents one's confidence in the certainty of the knowledge of the values of some parameters/variables. These can be either observables that can be measured or theoretical parameters whose values are to be inferred. The aim of the Bayesian analysis, in the present context, is the construction of the posterior PDF of the distances of the data points, the set of the Fourier modes that define the density and velocity fields, and σ_{NL} , given Cosmicflows-like data and under the assumption of the ΛCDM model. More specifically, the posterior PDF is calculated within the linear approximation of the ΛCDM model, with the Planck parameters (Ade et al. 2016). A mild non-linear correction is added to the linearly calculated velocity field whose amplitude is controlled by σ_{NL} (to be defined later), whose magnitude is to be estimated as well.

The Bayesian posterior PDF is numerically evaluated by means of the MCMC sampling. Given the posterior PDF the mean and variance of the desired density and velocity fields are readily calculated, much in the same way as in the WF/CRs formalism (Zaroubi et al. 1995). The main difference between the WF/CRs and the MCMC cases is that in the former the posterior PDF is assumed to be known analytically and in the later it is evaluated numerically.

2.1 Bayesian posterior PDF and likelihood function

Bayes' theorem states that the posterior PDF, of the model given the observed data, is the product of the conditional probability of the data given the model, hence the likelihood function, times the prior probability of the model, normalized by the evidence. In the language of Bayes' theorem the distribution of the true distances of the data points, the ensemble of the Fourier modes and σ_{NL} consist the multi-parameter model whose parameters are to be estimated given the data. The ΛCDM cosmological model provides the framework within which that multi-parameter model is constructed. Neglecting

here the evidence the posterior PDF is:

$$P(\Delta_k, \mathcal{D}, \sigma_{\text{NL}} | \mathcal{M}, \mathcal{Z}) \propto L(\mathcal{M}, \mathcal{Z} | \Delta, \mathcal{D}, \sigma_{\text{NL}}) P(\Delta, \mathcal{D}, \sigma_{\text{NL}}) \quad (1)$$

Here $\mathcal{D} = \{d_i\}$ (proper distances of the data points, $i = 1, \dots, n$ where n is the number of data points), $\Delta_k = \{\delta_k\}$ (the ensemble of the Fourier modes, where $\delta_k = FT(\delta(\mathbf{r}))$ is the Fourier transform of the fractional over-density field $\delta(\mathbf{r})$) and σ_{NL} are the output variables/parameters to be estimated. $\mathcal{Z} = \{z_i\}$ (observed redshifts of the data points) and $\mathcal{M} = \{\mu_i\}$ (observed distance moduli) are the input observed data. $L(\mathcal{M}, \mathcal{Z} | \Delta, \mathcal{D}, \sigma_{\text{NL}})$ is the likelihood function and $P(\Delta, \mathcal{D}, \sigma_{\text{NL}})$ is the prior.

The errors on the observed data points are assumed to be independent, and so are the errors on the redshift and distance modulus of a given galaxy. All observational errors are assumed to be normally distributed. The likelihood function is thus the product of n likelihood functions, one for each of the i constraints used. Furthermore, given that the redshifts and distance moduli are independent, the i -th likelihood function is a product of two independent likelihood functions denoted here by $L_i^{\nu_r}$, associated eventually with the velocity of the data point (Eq. (7) below) and L_i^{μ} . The likelihood function is:

$$L(\mathcal{M}, \mathcal{Z} | \Delta, \mathcal{D}, \sigma_{\text{NL}}) = \prod_i^n L_i^{\mu}(\mu_i | \Delta, \mathcal{D}, \sigma_{\text{NL}}) L_i^{\nu_r}(z_i | \Delta, \mathcal{D}, \sigma_{\text{NL}}) \quad (2)$$

2.2 The Likelihood function: distances

Given a Gaussian error $\sigma_{\mu,i}$ on the measurement, L_i^{μ} is written:

$$L_i^{\mu}(\mu_i | d_i) = \frac{1}{\sqrt{2\pi\sigma_{\mu,i}^2}} \exp\left(-\frac{(\mu_i - \mu(d_i))^2}{2\sigma_{\mu,i}^2}\right) \quad (3)$$

where

$$\mu(d) = 5 \log_{10} \left(\frac{d_L(d)}{10 \text{pc}} \right), \quad (4)$$

where $d_L(d)$ is the luminosity distance associated with the proper distance d .

$$d_L(d) = d(1 + \bar{z}(d)) \quad (5)$$

and to 2nd order the cosmological redshift (\bar{z}) corresponding the proper distance d is given by:

$$\bar{z}(d) = \frac{2}{3\Omega_0} \left(1 - \sqrt{1 - \frac{3\Omega_0 H_0 d}{c}} \right) \quad (6)$$

Here Ω_0 is the matter density parameter, H_0 is Hubble's constant evaluated at the present epoch and c is the speed of light.

2.3 The Likelihood function: velocities

The velocity of the i -th data point is related to its observed redshift via

$$v_{r,i}^{\text{obs}} = c \frac{z_i - \bar{z}(d_i)}{1 + \bar{z}(d_i)}. \quad (7)$$

Given the ensemble of Fourier modes, Δ_k , the assumed cosmological 3D velocity field is given by the following inverse Fourier transform,

$$\mathbf{v}(\mathbf{r} | \Delta_k) = FT^{-1} \left(-i H_0 f(\Omega_0) \frac{\mathbf{k}}{k^2} \delta_k \right), \quad (8)$$

where $f(\Omega_0)$ is the linear growth factor. One should note here that $\mathbf{v}(\mathbf{r} | \Delta_k)$ is the velocity field predicted by the linear theory from a given over-density field $\delta(\mathbf{r})$.

Our aim here is to reconstruct the LSS from the grouped version of a Cosmicflows-like catalog of galaxy velocities. A grouped catalog means here a catalog in which all galaxies belonging to a group or cluster of galaxies are collapsed onto one data points. The grouping acts as a smoothing process of the internal virial velocities and thereby serve as a filter of non-linear velocities. The following crude approximation is introduced here to account for the residual non-linear component of the observed data. The full velocity field is assumed to include a non-linear component:

$$\mathbf{v}^{\text{full}}(\mathbf{r}) = \mathbf{v}(\mathbf{r} | \Delta_k) + \mathbf{v}^{\text{NL}}(\mathbf{r}) \quad (9)$$

The non-linear component, $\mathbf{v}^{\text{NL}}(\mathbf{r})$, is assumed to constitute a white noise with a variance given by:

$$\sigma_{\text{NL}}^2 = \langle \mathbf{v}^{\text{NL}}(\mathbf{r})^2 \rangle. \quad (10)$$

The likelihood function for the observed redshift is readily written here in terms of the observed velocity:

$$L_i^{\nu_r}(z_i | \Delta_k, \mathcal{D}, \sigma_{\text{NL}}) = \frac{1}{\sqrt{2\pi\kappa_i^2}} \exp\left(-\frac{\left(v_{r,i}^{\text{obs}} - \mathbf{v}(d_i \hat{\mathbf{r}}_i | \Delta_k) \cdot \hat{\mathbf{r}}_i\right)^2}{2\kappa_i^2}\right) \quad (11)$$

where $\hat{\mathbf{r}}_i$ is the unit vector in the direction of the i -th data point and

$$\kappa_i^2 = \sigma_{\text{NL}}^2 + \frac{\sigma_{c z,i}^2}{(1 + \bar{z}(d_i))^2}. \quad (12)$$

2.4 Priors

The elements of the model under consideration are the Fourier modes, the distribution of the distances of the data points and σ_{NL} . Hence the joint prior of the model is written as:

$$P(\Delta_k, \mathcal{D}, \sigma_{\text{NL}}) = P(\Delta_k) P(\mathcal{D}) P(\sigma_{\text{NL}}). \quad (13)$$

The Fourier modes are evaluated on a discrete grid which is written here symbolically as $\{\mathbf{k}_j\}$, where $j = 1, \dots, m$ where m is the number of the Fourier modes. The prior of the ensemble of the Fourier modes is:

$$P(\Delta_k) = \prod_{j=1}^m \frac{1}{2\mathcal{P}(k_j)} \exp\left(-\frac{|\delta_{\mathbf{k}_j}|^2}{\mathcal{P}(k_j)}\right) \quad (14)$$

Here $\mathcal{P}(k)$ is the Λ CDM power spectrum at wave number k . Writing the prior on the distances is complicated and somewhat ad hock (see extensive description in [Graziani et al. 2019](#)). We opt for a simple description based on the fact that the redshift distance, d_z is a good proxy to the actual distance for all but the very nearby data points:

$$d_z = \frac{c}{H_0} \int_0^z \frac{d\bar{z}}{\sqrt{\Omega_m(1 + \bar{z})^3 + (1 - \Omega_m)}}. \quad (15)$$

A histogram of the distribution of the redshift distances, $N_{d_z}^{\text{obs}}$ is constructed from the distribution of the observed redshifts and is taken to be a good proxy to the histogram of the distribution of the true distances. Hence, the prior of the true distance is approximated by:

$$P(\mathcal{D}) = \prod_{i=0}^n N_{d_z}^{\text{obs}}(d_i). \quad (16)$$

3 HAMILTONIAN MONTE CARLO SAMPLING

Given the posterior PDF (Eq. (1)) the inference of the LSS from the data and the assumed prior is well posed and in principle can be readily calculated. Yet, the treatment of the distances of the data points as part of the parameters of the model to be inferred makes the problem of inference intractable analytically. This leaves numerical sampling of the posterior PDF as the only viable way for calculating the mean and variance, say, of the density and velocity fields given the data and the prior. The very large numbers of the parameters of the model, the so-called the curse of dimensionality, calls for sophisticated sampling methods, where the sampling is done by random Markov chains generated by random Monte Carlo realizations. The construction of Markov chains often follows the the Metropolis-Hastings or the Gibbs algorithms. Yet, the numerical efficiency and the slow convergence of these algorithms limit their applicability to very high dimensional cases.

The HMC is an algorithm that enables an efficient sampling of complex posterior PDFs of high dimensionality models and large input databases. There is ample evidence in the literature that the exploration provided by HMC methods is order of magnitudes more efficient than the Metropolis-Hastings or even the Gibbs sampling. The reader is referred to the excellent review of the HMC method and its comparison with other MCMC sampling methods of Neal (2011) and in particular to Jasche & Kitaura (2010) and Jasche & Lavaux (2019, and references therein) for the applications of HMC to the reconstruction of the LSS from redshift surveys.

3.1 Hamiltonian trajectories in phase space

A detailed presentation of the MCMC sampling in general and the HMC sampling in particular of the posterior PDF is beyond the scope of the paper. Only the key general elements of the HMC are given here. The parameters of the model are denoted here by:

$$\mathbf{q} = \{q_a\} = (\delta_{k,1}^R, \dots, \delta_{k,m}^R, \delta_{k,1}^I, \dots, \delta_{k,m}^I, d_0, \dots, d_n, \sigma_{\text{NL}}) \quad (17)$$

Here, the real and imaginary components of the complex $\delta_k = \delta_k^R + i\delta_k^I$ are denoted as separate parameters. For the sake of the clarity of the presentation we define here the posterior function as $\Pi(\mathbf{q}) = P(\Delta_k, \mathcal{D}, \sigma_{\text{NL}} | \mathcal{M}, \mathcal{Z})$.

A Hamiltonian system is defined by means of associating $\Pi(\mathbf{q})$ with a potential of classical particles, $\Psi(\mathbf{q})$,

$$\Psi(\mathbf{q}) = -\ln \Pi(\mathbf{q}). \quad (18)$$

The parameters $\{q_a\}$ are assumed to consist a set of canonical coordinates. These are supplemented by auxiliary quantities, referred to as their associated momenta, $\mathbf{p} = \{p_a\}$ and a 'mass matrix' M . The dynamics of this Hamiltonian system is governed by the Hamiltonian,

$$H(\mathbf{p}, \mathbf{q}) = \frac{1}{2} \mathbf{p}^T M^{-1} \mathbf{p} + \Psi(\mathbf{q}) \quad (19)$$

The equations of motions of the \mathbf{q} and \mathbf{p} are given by Hamilton equations:

$$\begin{aligned} \frac{dp_a}{dt} &= -\frac{\partial H}{\partial q_a} = -\frac{\partial \Psi(\mathbf{q})}{\partial q_a}, \\ \frac{dq_a}{dt} &= \frac{\partial H}{\partial p_a} \end{aligned} \quad (20)$$

Considering these Hamiltonian system as a many body system,

probability distribution function of \mathbf{q} and \mathbf{p} , $\Pi(\mathbf{q}, \mathbf{p})$ is related the the Hamiltonian via:

$$\Pi(\mathbf{q}, \mathbf{p}) \propto \exp(-H(\mathbf{q}, \mathbf{p})) = \Pi(\mathbf{q}) \exp\left(-\frac{1}{2} \mathbf{p}^T M^{-1} \mathbf{p}\right). \quad (21)$$

This is a key result. There is no cross-correlation between the distributions of the coordinates and the momenta in the joint PDF $\Pi(\mathbf{q}, \mathbf{p})$. It follows that the Hamiltonian trajectories properly sample the desired posterior PDF of the parameters of the model under consideration.

3.2 Construction of HMC chains

A chain starts with the coordinates and momenta randomly drawn and serve as the initial conditions for the integration of equations of motion (Eq. (19)). These are integrated over a pseudo time τ . The final position of that trajectory in the $\{\mathbf{q}, \mathbf{p}\}$ phase space, is the candidate state. If endpoint failed the standard Metropolis-Hastings acceptance rule, the integration starts all over with the same initial coordinates but with new randomly drawn momenta. If the endpoint passed the acceptance rule, that trajectory becomes a step along the chain. The next step starts with the coordinates (\mathbf{q}) accepting the final coordinates from the last step and the momenta (\mathbf{p}), on the other hand, are again randomly drawn. The final positions of the successive trajectories form the chain.

3.3 Integrating the HMC trajectories

If the integration can be done analytically, the Hamiltonian framework insures an acceptance rate of 1, namely all candidate states are accepted, even when candidates are far to the current position. However, for most problems, analytical integration is impossible and numerical solvers must be used. The integrator of choice is the Leapfrog algorithm, which insures ergodicity, namely the conservation of the Hamiltonian. This insures that the error introduced when computing the trajectory depends only on the integration step size and not on the number of integration steps. In other words, the use of the Leapfrog algorithm yields stable trajectories. In practice, this stability is limited by the numerical precision of the derivatives $\left(\frac{\partial \ln \Pi(\mathbf{q})}{\partial q_a}\right)$. Thus, the HMC is only applied to models where these derivatives can be computed analytically, which is the case for this work.

Note that trajectory length is simply the product of the step size and the number of steps used in the (leapfrog) integration. In this context, the acceptance rate for a given state is only a function of the step size. Therefore the step size can be tuned in order to obtain a given acceptance rate. Studies in the literature (e.g. Hoffman & Gelman 2011) advocate that an acceptance rate of 0.65 (used here) provides an optimal balance between computational resource usage and exploration. Hoffman & Gelman (2011) introduced the ‘‘Dual Averaging’’ method that dynamically tunes the step size to reach any given acceptance rate. The step size set to achieve this acceptance rate depends on the complexity of the problem: the more complex the problem and the more correlated the variables, the smaller the step size must be.

Secondly, since the integration is ergodic, every trajectory ultimately returns to the initial state (to within integration error). This is problematic since such closed orbits return a final state identical to the initial state resulting in no additional knowledge of the parameter space (and a waste of computational resources in the process). Therefore it is absolutely critical that the integration is halted

after a designated number of steps, specifically chosen such that the candidate state is the furthest away from the initial position. At this maximum, the trajectory starts turning back towards the initial state. Depending strongly on the initial momentum, this value is different for each trajectory. Several methods have been developed to automatically tune this parameter, the most well known being the No U-Turns (NUTS) algorithm proposed in [Hoffman & Gelman \(2011\)](#), whose detail is out of the scope of this paper. NUTS and the “Dual averaging” technique can be used together.

3.4 The Mass matrix

Consider the classical dynamics described by Eq. (20) - a trajectory evolves from a random position in the multi-dimensional phase space towards a local minimum of the potential $\Psi(\mathbf{q})$. In the presence of dissipative forces, the trajectory would reach a local minimum of the potential and stay there. For a Hamiltonian system whose energy is conserved, the trajectory oscillates around the local minimum with an amplitude dictated by the energy of the system and its mass. As the energy of each trajectory is set by the random choice of its initial momentum. The statistics of these initial momenta is encoded in the mass matrix. The selection of a mass matrix influences heavily the efficiency of the exploration and the rapidity of the convergence. Asymptotically however, it does not bias nor modify the result. Even though there is theoretically no optimal choice of mass matrix, using the covariance of the parameters is the canonical approach. This covariance matrix is however a priori not known and has to be estimated.

In the absence of observational data the posterior PDF degenerates into the prior PDF and the model parameters (\mathbf{q}) are all statistically independent and their statistical behaviour is fully understood. The real and imaginary components of the Fourier modes are normally distributed around zero with a variance given by the power spectrum (see [Jasche & Kitaura 2010](#), for further discussion). The proper distances are distributed around the corresponding redshift distances with a variance given by $(\sigma_V/H_0)^2$ (where σ_V is the Λ CDM one dimensional velocity dispersion). The choice of the size of the other parameters (limited to σ_{NL} in this work) has to be estimated more freely.

The mass matrix for the trivial case of no observational data, namely the posterior equals the prior PDF, is thus written as:

$$M_{ab}^{-1} = I_{ab} \times \begin{cases} \mathcal{P}(k_a)/2 & \text{if } a \leq m \\ \mathcal{P}(k_{a-m})/2 & \text{if } m < a \leq 2m \\ \sigma_v^2/H_0^2 & \text{if } 2m < a \leq 2m+n \\ 1 & \text{if } a = 2m+n+1 \end{cases} \quad (22)$$

where I is the identity matrix and k_a is the wavenumber of the Fourier mode $\delta_{k,a}$. The mass matrix of Eq. (22) is used here in the general case, where the estimation is done given the data and the prior.

3.5 Sampling by HMC chains

An HMC chain is made up of a set of steps, often hundreds of these, which mark the endpoints of Hamiltonian trajectories. Typically, the HMC algorithm is “ergodic” — it is not trapped in some sub-volume of the phase space but has a finite probability of visiting any volume element of phase space. Moreover, the property of detailed balance of the HMC chains (see [Neal 2011](#)) insures the probability of a chain to visit the volume element $d\mathbf{q}$ equals $\Pi(\mathbf{q})$. Namely,

HMC chains sample the parameters space (\mathbf{q}) with the desired posterior probability. This leads to the practical use of the HMC sampling to estimate the parameters of the model given the data and the prior. Consider an HMC chain S , $\mathbf{q}(s) = \{\mathbf{q}_1, \dots, \mathbf{q}_{n_S}\}$, and some functional of the parameters of the model $F(\mathbf{q})$, then the conditional mean value of $F(\mathbf{q})$ given the data and the prior is given by:

$$\langle F(\mathbf{q}) \mid \text{data, prior} \rangle = \int F(\mathbf{q})\Pi(\mathbf{q})d\mathbf{q} \approx \frac{1}{n_S} \sum_{s=1}^{n_S} F(\mathbf{q}_s). \quad (23)$$

A further use of HMC chains is the construction of constrained realizations of the parameters \mathbf{q} , given the data and the prior. Namely, the generalization of constrained realizations of Gaussian random fields ([Bertschinger 1987](#); [Hoffman & Ribak 1991](#)) to the general case of non-Gaussian posterior PDFs. This is done by selecting states on a given chain that are well separated along the chain, so to insure their statistical Independence.

4 TECHNICAL IMPLEMENTATION

An HMC algorithm computationally outperforms the more traditional Metropolis - Hastings and Gibbs sampling algorithms. This is also the case with the problem, of the reconstruction of the LSS from a CF3-like catalogue, addressed here and by [Graziani et al. \(2019\)](#) which used the Gibbs sampling approach. Quantifying the speed-up of the HAMLET method compared to that of [Graziani et al. \(2019\)](#) is complicated because there are differences to both the implementation (compiled on GPUs versus interpreted on a single CPU) and the algorithm (HMC versus Gibbs sampling). It is thus not straight forward to identify exactly which aspect of the HAMLET method is mostly responsible for the increase in efficiency. A quick comparison shows that the HAMLET code outperforms the code of [Graziani et al. \(2019\)](#) by several orders of magnitude (between 3 to 4) in speed while fitting orders of magnitudes more parameters ($\sim 2 \times 10^6$ versus $\sim 4.5 \times 10^4$). For example, in the case of reconstructing the LSS from the $\sim 1.5 \times 10^4$ constraints provided by the grouped CF3 catalogue, the MCMC method of [Graziani et al. \(2019\)](#) takes more than a month compared with the HAMLET which takes on the order of 10 minutes. The increase in speed is a necessary condition for future applications of the HAMLET code. One such application is the setup of constrained initial conditions for high resolution cosmological simulations (cf. [Libeskind et al. 2020](#)), for which the number of the needed Fourier modes is much larger than what is used here. Also, the upcoming 4th Cosmicflows data release (CF4) is expected to roughly triple the size of the CF3 data. Preliminary analysis suggests that HAMLET will be capable in exploiting the CF4 data.

A brief review of the computational implementation of the HAMLET code follows. It takes advantage of a number of highly-abstract layers as implemented by open-source Python libraries `tensorflow` and `tensorflow-probabilities`. The `tensorflow` library provides a framework that enables a python code to transparently scale on multiple CPUs and/or GPUs and to be compiled at run time, while the `tensorflow-probabilities` provides a plug-and-play implementation of the HMC, NUTS and other tools to run and analyse MCMC chain. While the gradient of the the posterior PDF, can be extremely tedious to write by hand, `tensorflow` is capable of transparently computing it, by constructing a complex derivation graph that can be very efficiently evaluated. Only the gradient of the inverse of the Fourier transform had to be constructed.

5 TESTING HAMLET AGAINST A LINEAR MOCK COSMICFLOWS-3 SURVEY

The HAMLET algorithm is tested against a CF3-like survey drawn from a linear random realization of the density and velocity fields, constructed within the framework of the Λ CDM model. The selection of the data points and the assignment of the observational errors replicate the selection and the errors of the actual CF3 data. Our aim here is to test the the HAMLET algorithm and its performance in the ideal case where in the limit of perfect data - densely, homogeneously and isotropically sampled and with negligible errors - the HAMLET should accurately recover the input density and velocity fields (cf. [Graziani et al. 2019](#)). Testing HAMLET against a mock non-linear CF3 database is presented in Valade, Libeskind and Hoffman (to be submitted)

5.1 Mock Catalogue construction

A linear realization of a Gaussian random field, defined by the Λ CDM power spectrum and cosmological parameters ([Ade et al. 2016](#)) is used here as a base for our mocks. The field is constructed on a 128^3 Cartesian grid within a box with side length $L = 500h^{-1}$ Mpc. Periodic boundary conditions are assumed. A random observer is selected to reside at the center of the computational box and a mock Supergalactic coordinate system is assigned centered on the observer and aligned with the principal directions of the grid. A mock catalog consists of Supergalactic latitude (SGB) and longitude (SGL), distance modulus (μ), its error (σ_μ), the redshift (z) and its error (σ_{cz}).

Fig. 1 presents the “target” density and velocity field, from which the mock data has been drawn and which the HAMLET algorithm is designed to recover. The linear over-density (δ) and the radial component of the velocity field (v_r) are depicted. The target field is smoothed with a Gaussian kernel of a radius of $5h^{-1}$ Mpc.

The constraints are isotropically selected within a sphere of radius of $160h^{-1}$ Mpc. A radial selection function is imposed so as to have a uniform distribution per radial distance bins, $P(d) = \text{constant}$, where distances are measured with respect to the mock observer at the relative centre of the box. This choice is motivated by the relative flatness of the redshift distance distribution of the CF3 grouped data points (Fig. 2). The $160h^{-1}$ Mpc cut corresponds to the effective distance cut of the CF3 data. The errors assigned to the mock data points follow the redshift distribution of the errors of the actual CF3 data. The following procedure is used. Given a mock point it inherits the error of the actual CF3 data point that is closest to it in redshift.

The two main factors that affects the quality of the Bayesian reconstruction in general and the HMC in particular are the numbers of the data points and their associated errors. In the limit of very dense sampling of the data points and negligible errors the target field should be reconstructed with high fidelity. In the other extreme case of very sparse sampling and large observational uncertainties, the null field predicted by the prior PDF is recovered. An ensemble of 9 different mock databases has been constructed so as to investigate how these two factors affect the outcome of the HAMLET reconstruction. Three different numbers of data points are selected, $(7.5, 15, 30) \times 10^4$. The distance moduli errors are gauged by an α parameter, $\sigma_\mu = \alpha \sigma_\mu^{\text{CF3}}$, where σ_μ^{CF3} is the value for the actual CF3 survey error¹. In otherwords $\alpha = 1$ corresponds to the typical

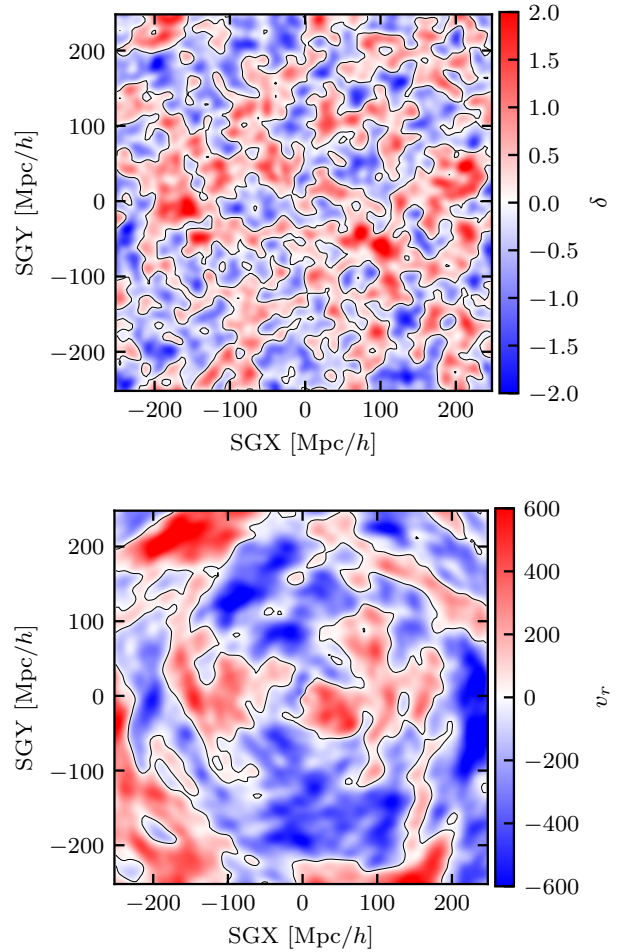


Figure 1. A slice through the over-density (δ , upper panel) and the radial component of the velocity fields (v_r , lower panel) of the target field. The mock observer is located at the origin of the coordinate system. The color bars present the color coding of the presented fields. Velocities are in units of km/s. The contour lines correspond to the zero values of the two fields. The target field is Gaussian smoothed with a kernel of $c 5h^{-1}$ Mpc.

errors associated with the inherent uncertainty in scaling relations (eg. Tully-Fisher) distance measures, while $\alpha = 1/10$ is meant to mimic a catalogue constructed entirely with more accurate distance measures, like TRGB or SuperNovae. The 9 mock databases are assigned the 3 different numbers of data points and 3 different α values (Table 1). The case of 1.5×10^4 data points and $\alpha = 1$ corresponds most closely to the grouped CF3 data.

A note of caution on the expected effect of the sharp drop has on the Bayesian reconstruction is due here. [Hinton et al. \(2017\)](#) have investigated this exact problem: the effect that a sample selection function with a sharp cutoff has on the likelihood function and thereby on the Bayesian posterior PDF. Their conclusion is that the inferred variables close to the edge of the data, namely close to the cutoff, are biased. Our analysis and findings support the finding of

candles since e.g. the error on a distance obtained from the Tip of the Red Giant Branch method is around 5% while from scaling relations are closer to 20%. Thus a catalogue of just TRGB distances would correspond to $\sigma_\mu = 0.25$ with respect to CF3 which is scaling relation dominated.

¹ Varying σ_μ is meant to mimic the different precision of different standard

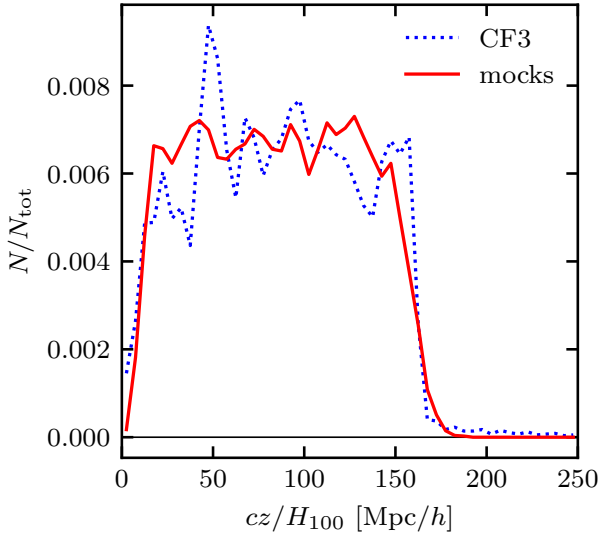


Figure 2. The “selection function” i.e. the distribution of the distances for the sample of points used as constraints. For comparison we also show CF3.

Table 1. Mock catalogues and their characteristics

Name	N of points	α , Factor on σ_μ
CF3+ like	15 000	1
Better measurements	15 000	1/2
Very good measurements	15 000	1/10
More measurements	30 000	1
More, better measurements	30 000	1/2
More, very good measurements	30 000	1/10
Fewer measurements	7 500	1
Fewer, better measurements	7 500	1/2
Fewer, very good measurements	7 500	1/10

Hinton et al. (2017). Consequently we limit our analysis and present results only within a sphere of a radius of $150h^{-1}$ Mpc.

5.2 Convergence

A critical issue that MCMC methods in general and the HMC in particular face is that of convergence, namely how long should an MCMC chain or HMC trajectory be to meet some given criteria of confidence in the estimated parameters. (The discussion that follows focuses on HMC trajectories but it implies to MCMC chains in general.) The HMC trajectories never ‘rest’ and keep on ‘moving’ in the parameters space. Three obvious issues to consider are: a. Does the HMC trajectory oscillate around the ‘true’ values of the parameters, namely the issue of bias; b. What is the scatter exhibited by the trajectory, i.e. the variance around the mean (defined by Eq. (23)); c. What is the rate of convergence. The convergence rate is discussed here and the issues of bias and variance are addressed in subsections 5.3 and 5.5 below.

The rate of convergence is examined here by monitoring the change of the mean of the density field, $\langle \delta \rangle$, along the HMC trajectory. Fig. 3 presents the differential change in $\langle \delta \rangle$ normalized by the (square root of the) cosmic variance between successive steps, $|\langle \delta \rangle / \Sigma_\delta)_s - (\langle \delta \rangle / \Sigma_\delta)_{s-1}|$. Here Σ_δ^2 is the variance of the δ field

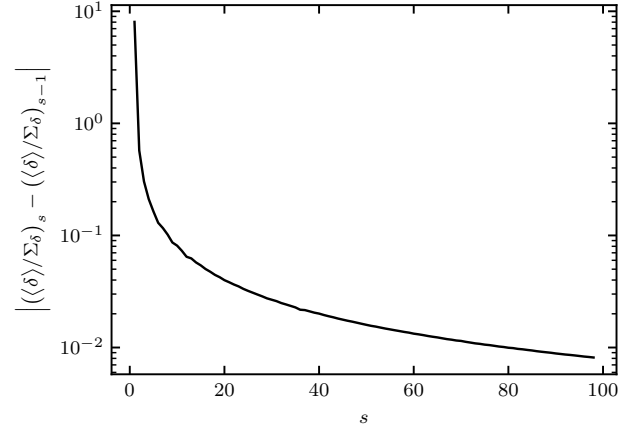


Figure 3. Differences between successive partial estimations of the signal over noise ratio field as a function of the number of steps used to estimate it. All mocks converge in a very identical way.

evaluated at a given step of the HMC. Fig. 3 indicates that to get to percent level convergence requires on the order of 100 chains.

5.3 Reconstruction of the large scale structure

The HAMLET method’s main mission is to perform a Bayesian estimation of the LSS, namely the density and velocity fields, from Cosmicflows-like databases. To meet that end and examine it we focus here on a subset of the \mathbf{q} parameters, $\mathbf{q}_{\text{LSS}} = (\delta_{k,1}^R, \dots, \delta_{k,m}^R, \delta_{k,1}^I, \dots, \delta_{k,m}^I)$, namely the ones that determine the LSS. The conditional mean field, given the data and the prior model is readily written (as a particular case of the general Eq. (23)) as:

$$\mathbf{q}_{\text{LSS}}^{\text{mean}} = \langle \mathbf{q}_{\text{LSS}} | \text{data, prior} \rangle \approx \frac{1}{n_S} \sum_{s=1}^{n_S} \mathbf{q}_{\text{LSS},s} \quad (24)$$

An ensemble of n_{IS} independent states (IS) of the HMC chain is constructed as well $\{\mathbf{q}_{\text{LSS},i}^{\text{IS}}\}$ ($i = 1, \dots, n_{\text{IS}}$). The conditional mean field and the ensemble of ISs are the HMC equivalent of the WF estimator and the ensemble of CRs of the WF/CRs algorithm.

Fig. 4 shows a slice of the δ field for the 9 different mock data sets (see Table 1). The presented density field is the conditional mean field given the data, namely $\delta^{\text{mean}} = \delta(\mathbf{q}_{\text{LSS}}^{\text{mean}})$. The grid of density maps reflects the change of quality of the data - more data points and smaller errors corresponding to better data. Degradation of the data leads to an attenuation of δ^{mean} . This a manifestation of the well known property of the Bayesian estimation - the worse the data the more biased the results are towards the null field predicted by the prior model (cf. Zaroubi et al. 1995). The grey lines represent the $\delta = 0$ contour of the target. The reader will note how similar these are to the the limit of small errors and large data set (i.e. Fig. 4(i)). Indeed, in general, the target and reconstructions $\delta = 0$ contours match for $\alpha = 1/10$, Fig. 4(g,h,i). In the case of the CF3 mock ($\alpha = 1$, 15,000 points, figure Fig. 4(b)), the target density contour is fairly accurately recovered in the inner regions, i.e. within around $50 - 60 h^{-1}$ Mpc. Examining the density field reconstructions “vertically” indicates that the single most important factor for obtaining an accurate density field reconstruction is the data quality. Namely: *Better data is more important than larger data sets.*

For a given catalogue size, better data allows the reconstruction to be accurate at greater distances. For a given error, more data improves the reconstructions at fixed distances, instead of extending the improvement of the reconstruction.

The linear over-density field constitutes a random Gaussian field whose variance is determined by the power spectrum of the field and the resolution of the given realizations of the field. This is the cosmic variance of the δ field, denoted by σ_δ^2 . The variance of different states along the HMC chain, Σ_δ^2 , varies according to the ‘strength’ of the data and the properties of prior model. Furthermore, it varies with the location at which it is evaluate. i.e. $\Sigma_\delta = \Sigma_\delta(\mathbf{r})$. The spatial variation of $\Sigma_\delta(\mathbf{r})$ reveals the constraining power of the data, given the prior model. Where $\sigma_\delta(\mathbf{r})/\Sigma_\delta \ll 1$ the density field is strongly constrained by the data and the prior model and only very small scatter is expected to be found around the mean field. Where $\Sigma_\delta(\mathbf{r})/\sigma_\delta \sim 1$ the field is essentially unconstrained by the data and the prior model. Fig. 5 presents the variation of normalized constrained variance, $\Sigma_\delta(\mathbf{r})/\sigma_\delta$, for the 9 mock databases presented in Fig. 4. Inspection of Fig. 5 reveals that for all the mock data considered the quality of the reconstruction degrades with the distances from the (mock) observer. This is a reflection of the degradation of the data with the distance - the magnitude of the errors increases and the density of data point decreases with distance. The picture of how the reconstruction degrades with distance as a function of data set size and error reinforces the conclusions drawn from Fig. 4 namely smaller errors on the data improves the reconstructions more than larger data sets. Small data sets with small errors are worth more than large data sets with large errors when examining the reconstructed density field.

Next, the radial component of the velocity field is investigated (Figs. 6 and 7). The velocity field power spectrum is ‘redder’ than that of the δ field, namely it has more power on long wavelength compared with the short one, hence the velocities effective correlation length is larger than that of the densities. Hence one expects the velocities to be more constrained by the data than the densities. This is clearly manifested by Fig. 6. A visual of how well the target’s $v_r = 0$ contour matches the reconstructed radial velocity field indicates that even in the case of CF3 like mock (ie Fig. 6b) the reconstructed velocity field is doing a good job at greater distances (e.g as compared with the δ field). The velocity field around large, distance concentrations of matter and voids is accurately reconstructed with HAMLET. We can qualitatively assess the superiority of the velocity field reconstruction as compared to the density field by examining Fig. 7 (and comparing to Fig. 5) which shows just how well similar the reconstructed velocity field is to the target.

5.4 Monopole and dipole

Global measures of the velocity field are given by the volume-weighted mean monopole and dipole moments of the velocity field in spheres of radius R (Hoffman et al. 2021, for details). The monopole moment is the mean of $-\nabla \cdot \mathbf{v}/H_0$, where the scaling by H_0 is introduced so as to make the expression dimensionless and proportional to the mean (linear) over-density within R . The minus sign is introduced so as to make the monopole within a sphere of R to be proportional to the mean over-density within that volume. The dipole moment is the (volume weighted) mean value of the velocity, namely it is the bulk velocity of a sphere of radius R . The variation of the monopole and dipole moments with depth provides a global measure of the underlying LSS of the universe, and as such they serve as good monitors of the quality of the HAMLET reconstruction.

Fig. 8 presents the variation with depth of the monopole (upper row) and the dipole (middle row) of the velocity field, namely the mean fractional over-density (δ) and the bulk velocity of a sphere of radius R . The lower row shows the alignment of the bulk velocity of the reconstructed and the target velocity fields. The dependence of the estimation of the radial profiles of the moments on the quality of the data is investigated. The profiles are shown as a function of the magnitude of the errors ($\alpha = (1.0, 0.5, \text{ and } 0.1)$) and of the number of data points, $N = (0.75, 1.5 \text{ and } 3.0) \times 10^4$. The profiles are presented by their mean and standard deviation taken over the ensemble of steps.

The plots of Fig. 8 are informative. With the exception of the behaviour of the monopole moment close to the edge of the data, $R \lesssim 150 h^{-1}\text{Mpc}$, where the reconstructed monopole exceeds that of the target one. The edge-of-the-data discrepancy is in line with the findings of Hinton et al. (2017). As for all the other cases they behave as expected. The mean HAMLET profiles deviation from the target profile and the scatter around the mean profiles grow with R and get smaller with the increase of the number of steps. A note is due here on the large scatter in the amplitude and alignment of the bulk velocity at $R \gtrsim 100 h^{-1}\text{Mpc}$, say. The bulk velocity of a sphere of radius R is induced by structures outside that radius. The target field is constructed within a box of side length of $L = 500 h^{-1}\text{Mpc}$ with periodic boundary condition, which renders the power within the box and outside these radii, and its constraining power to be rather small. This is manifested by the large scatter around the mean. The lesson to be learnt here is that the reconstruction of the bulk velocity on a given scale R needs to be done within boxes of L much larger than R .

5.5 Correlation Coefficients

Next, the fidelity of the HAMLET reconstruction is monitored by means of the scatter of the density and radial velocity fields evaluated in radial shells. The upper panel of Fig. 9 shows the mean and scatter of the density in spherical shells of width of $\Delta R = 10 h^{-1}\text{Mpc}$ for the 3 values of α and the 3 assumed sizes of the mock catalogue. The mean density of the target field is presented for reference. The disagreement at $R \lesssim 150 h^{-1}\text{Mpc}$ is again clearly manifested. Next the density field within the shells is examined by studying the correlation between the densities of individual voxels (grid cells) within the shells. The lower panel of Fig. 9 shows the (Pearson) correlation coefficients of the HAMLET reconstructed and the target densities. The correlation coefficient profiles are again plotted for the 3 levels of errors and the 3 ensembles of the HMC chain. In general, the HAMLET reconstruction follows the target quite well. In the limit of much data and small errors, the reconstruction is very close to the target.

Fig. 10 applies the analysis of Fig. 9 to the case of the radial velocity field. The mean and scatter of v_r within spherical shells (upper row) and the correlation coefficient with the target field (lower row) are presented in Fig. 10. As expected, the comparison of the 2 figures clearly shows that the (radial) velocity field is much more correlated than the density field. Smoothing the target and the reconstructed fields would make them much more correlated. Again, in the limit of much data and small errors the reconstructed velocity field is so accurate that a correlation coefficient of nearly 0.8 is obtained at $150 h^{-1}\text{Mpc}$. Obtaining a CF like catalogue with such large numbers of data points is already a reality in CF4. On the other hand, having small errors corresponding to $\alpha = 1/10$ is still slightly unrealistic, but not unimaginable with future purpose

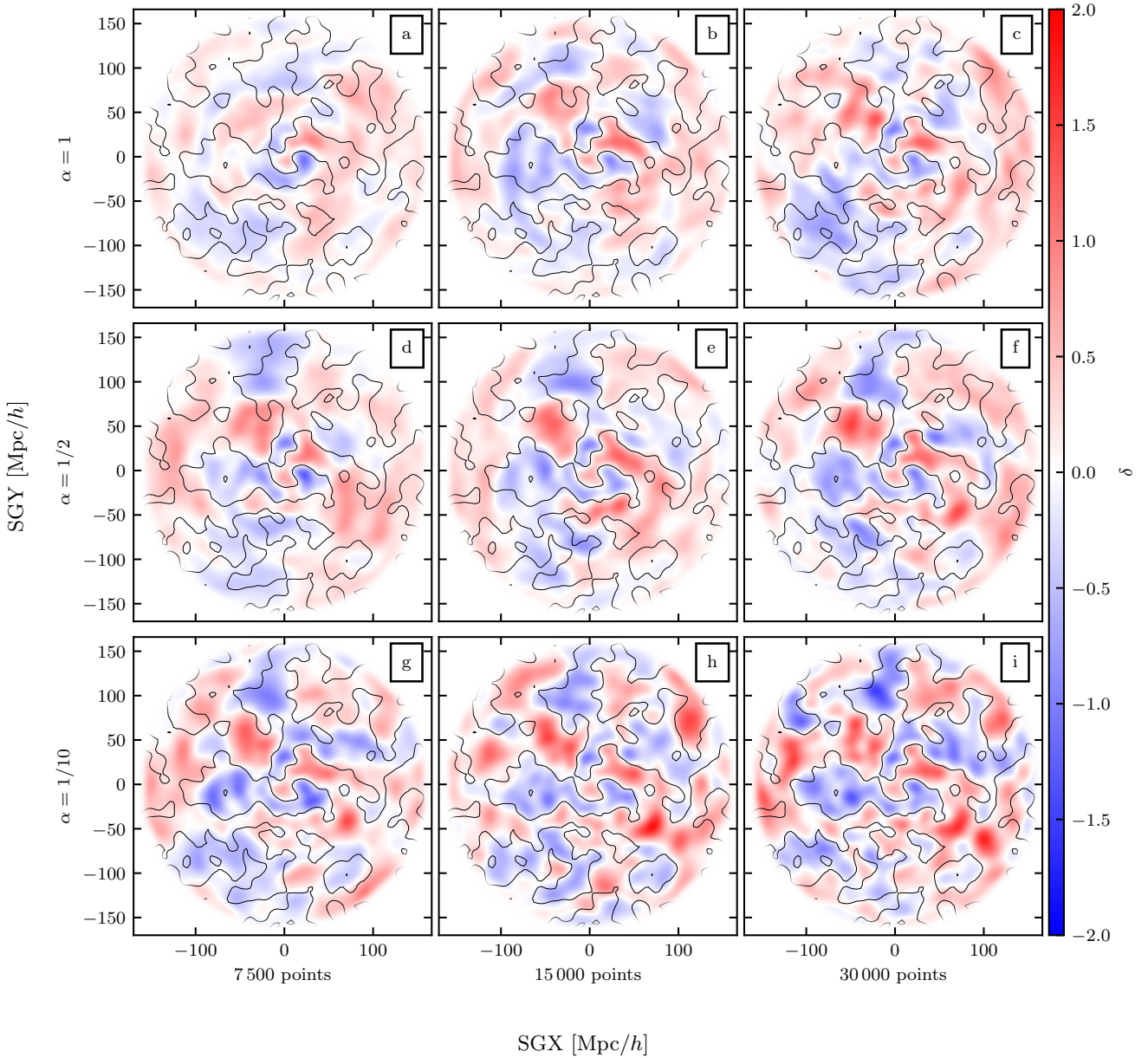


Figure 4. The conditional mean δ field given CF3-like mock data and the Λ CDM prior model. The field is Gaussian smoothed with a kernel of $5h^{-1}$ Mpc. The plots show color maps of a slice of the δ field. The color bar indicates the color coding of δ and the contour lines correspond to the zero level. The frames correspond to the different mock catalogs denoted by $(N/10^4, \alpha)$, where N is the number of data points and α controls the level of the observational errors, $\sigma_\mu = \alpha \sigma_\mu^{CF3}$. The nine mock data are: a. (0.75, 1.0), b. (1.5, 1.0), c. (3., 1.0); d. (0.75, 0.5), e. (1.5, 0.5), f. (3., 0.5); g. (0.75, 0.1), h. (1.5, 0.1), i. (3., 0.1). Frame **b** corresponds to the actual CF3 data in terms of the number of data points and the magnitude of the errors.

built telescopes designed specifically to monitor variable stars at cosmological distances.

6 SUMMARY AND DISCUSSION

The problem of the reconstruction of the large scale density and velocity fields from peculiar velocities surveys is addressed here within a Bayesian framework. In particular, the reconstruction aims at Cosmicflows-like data where observational uncertainties are on the distance moduli, which results in a lognormal bias on the es-

timated distances and velocities. The Hamiltonian Monte carlo reconstruction of the Local Environment (HAMLET algorithm performs the reconstruction within the framework of the linear theory of the Λ CDM standard cosmological model, which is taken here as the Bayesian prior, using the Hamiltonian Monte Carlo (HMC) method to sample the posterior probability distribution function (PDF) given the Λ CDM model and the Cosmicflows-like data. Like previous MCMC treatments of the problem (Lavaux 2016; Graziani et al. 2019) the HAMLET samples the posterior PDF of true distance of the data points coupled with the underlying linear density field. This differs from the Wiener filters and constrained

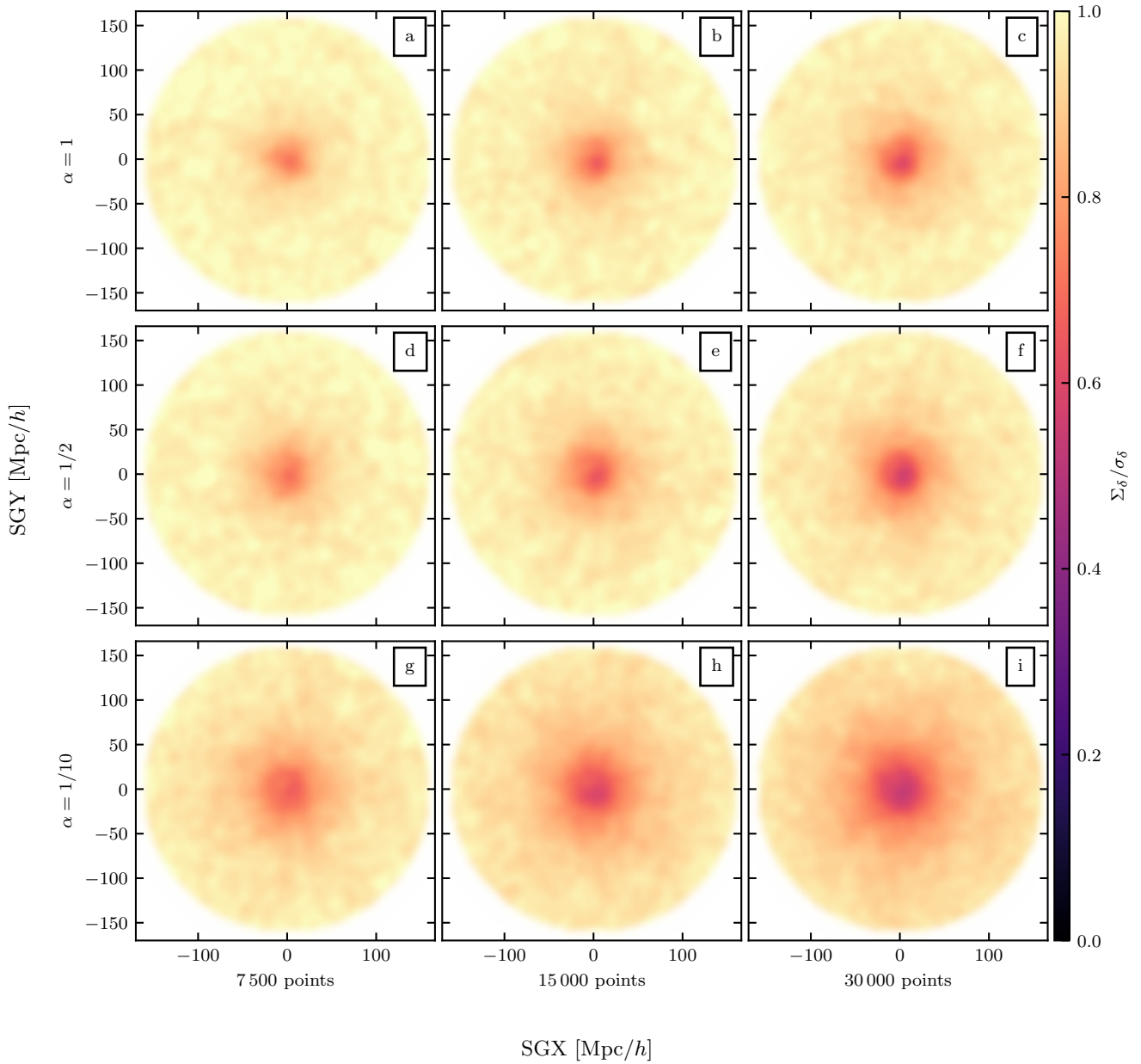


Figure 5. Color maps of the local constrained variance normalized by the cosmic variance of the δ field, $\sigma_\delta(\mathbf{r})/\Sigma_\delta$. The conventions and structure of Fig. 4 are followed here,

realizations (WF/CRs) approach where the correction of the log-normal bias is done independently of the Bayesian reconstruction of the LSS (Sorice 2015; Hoffman et al. 2021).

The current HAMLET HMC algorithm and the Lavaux (2016); Graziani et al. (2019) MCMC ones are formulated within the same mathematical Bayesian framework, making similar assumptions on the prior PDF and deriving the same posterior PDF from the same input data. The main difference between the standard (e.g. Metropolis-Hastings or Gibbs sampling) MCMC algorithm and the HMC is in the sampling of the posterior PDF. The extremely low rejection rate of the HMC steps and its ability to be run on GPUs, makes the procedure very efficient. A comparison of the performance of the HAMLET algorithm with the one presented in Graziani et al. (2019)

finds an efficiency gain factor of two to four orders of magnitude in favor of the HMC. This gain in efficiency will enable a very significant increase of resolution in future applications of the HAMLET algorithm compared to the resolutions used in the MCMC cases (Lavaux 2016; Graziani et al. 2019).

The successful application of the HAMLET algorithm to Cosmicflows-like mock data paves the way for its application to the actual Cosmicflows-3 data (Tully et al. 2016) and the upcoming next data release of Cosmicflows. Four immediate specific goals that can be achieved by such an applications are: 1. The reconstruction of the present epoch large scale velocity field, including the bulk velocity of the local volume; 2. The construction of constrained initial conditions of cosmological simulations, following

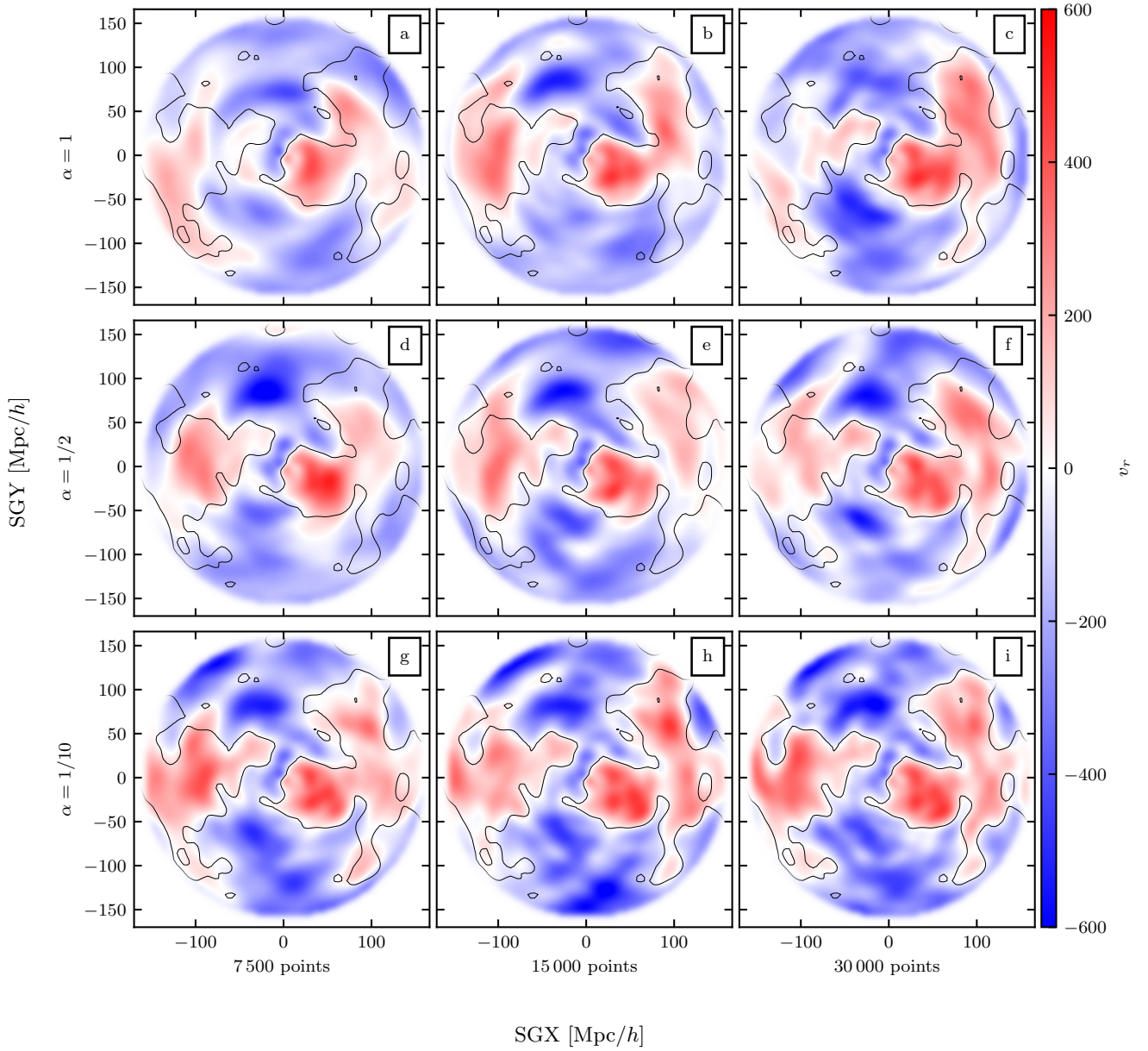


Figure 6. Same as Fig. 4 but for the radial component of the velocity field.

earlier studies that have the WF/CRs algorithm (e.g. Yepes et al. 2014; Sorce et al. 2016; Libeskind et al. 2020); 3. Adding to the list of parameters of the Bayesian model (Eq. (17)) cosmological parameters such as H_0 and the σ_8 normalization of the power spectrum, and estimating these self-consistently from data; 4. Studying the internal consistency of the different components of the Cosmicflows data, such as the zero-point calibration of the different data types of the Cosmicflows. This can be done by assigning different Hubble parameters to the different data sub-sets, and estimating them by Bayesian inference.

A few days before the submission of the current paper we came across the Boruah et al. (2021) preprint on the arXiv. The current and the Boruah et al.’s studies are similar - both address the problem of the reconstruction of the LSS from peculiar velocities surveys by means of HMC algorithms. The studies have been carried

out independently and have been applied to different data sets. A detailed comparison of the two will be presented elsewhere.

ACKNOWLEDGEMENTS

Useful discussions with Tamara Davis, concerning the Hinton et al. (2017) paper, are acknowledged. This work has been done within the framework of the Constrained Local Universe Simulations (CLUES) simulations. AV and NIL acknowledge financial support from the Project IDEXLYON at the University of Lyon under the Investments for the Future Program (ANR-16-IDEX-0005). YH has been partially supported by the Israel Science Foundation grant ISF 1358/18.

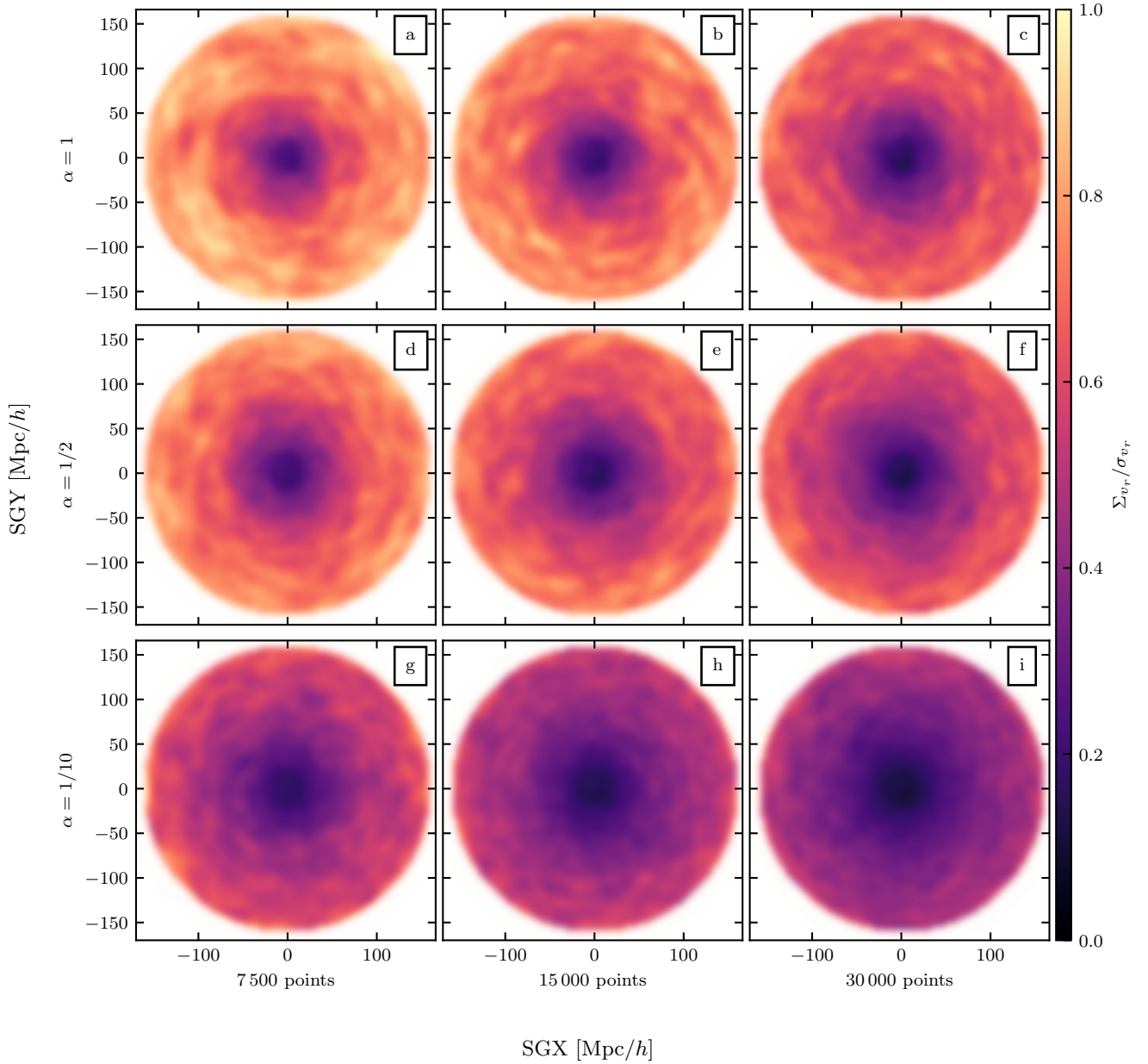


Figure 7. Same as Fig. 5 but for the radial component of velocity field ($v_r(\mathbf{r})$). The constrained and comoving variances are evaluated for $v_r(\mathbf{r})$.

DATA AVAILABILITY

The data underlying this article will be shared on reasonable request to the corresponding author.

REFERENCES

- Aaranson M., Huchra J., Mould J., Schechter P. L., Tully R. B., 1982, *ApJ*, **258**, 64
- Ade P. A. R., et al., 2016, *Astronomy & Astrophysics*, **594**, A13
- Bertschinger E., 1987, *ApJ*, **323**, L103
- Bertschinger E., Dekel A., 1989, *The Astrophysical Journal*, **336**, L5
- Boruah S. S., Lavaux G., Hudson M. J., 2021, arXiv e-prints, p. arXiv:2111.15535
- Dekel A., Silk J., 1986, *The Astrophysical Journal*, **303**, 39
- Graziani R., Courtois H. M., Lavaux G., Hoffman Y., Tully R. B., Copin Y., Pomarède D., 2019, *Monthly Notices of the Royal Astronomical Society*, **488**, 5438
- Hinton S. R., Kim A., Davis T. M., 2017, arXiv e-prints, p. arXiv:1706.03856
- Hoffman M. D., Gelman A., 2011, The No-U-Turn Sampler: Adaptively Setting Path Lengths in Hamiltonian Monte Carlo (arXiv:1111.4246)
- Hoffman Y., Ribak E., 1991, *ApJ*, **380**, L5
- Hoffman Y., et al., 2018, *Nature Astronomy*, **2**, 680
- Hoffman Y., Nusser A., Valade A., Libeskind N. I., Tully R. B., 2021, *MNRAS*, **505**, 3380
- Jasche J., Kitaura F. S., 2010, *MNRAS*, **407**, 29
- Jasche J., Lavaux G., 2019, *A&A*, **625**, A64
- Lavaux G., 2016, *MNRAS*, **457**, 172
- Libeskind N. I., et al., 2020, *Monthly Notices of the Royal Astronomical Society*, **493**, 4538

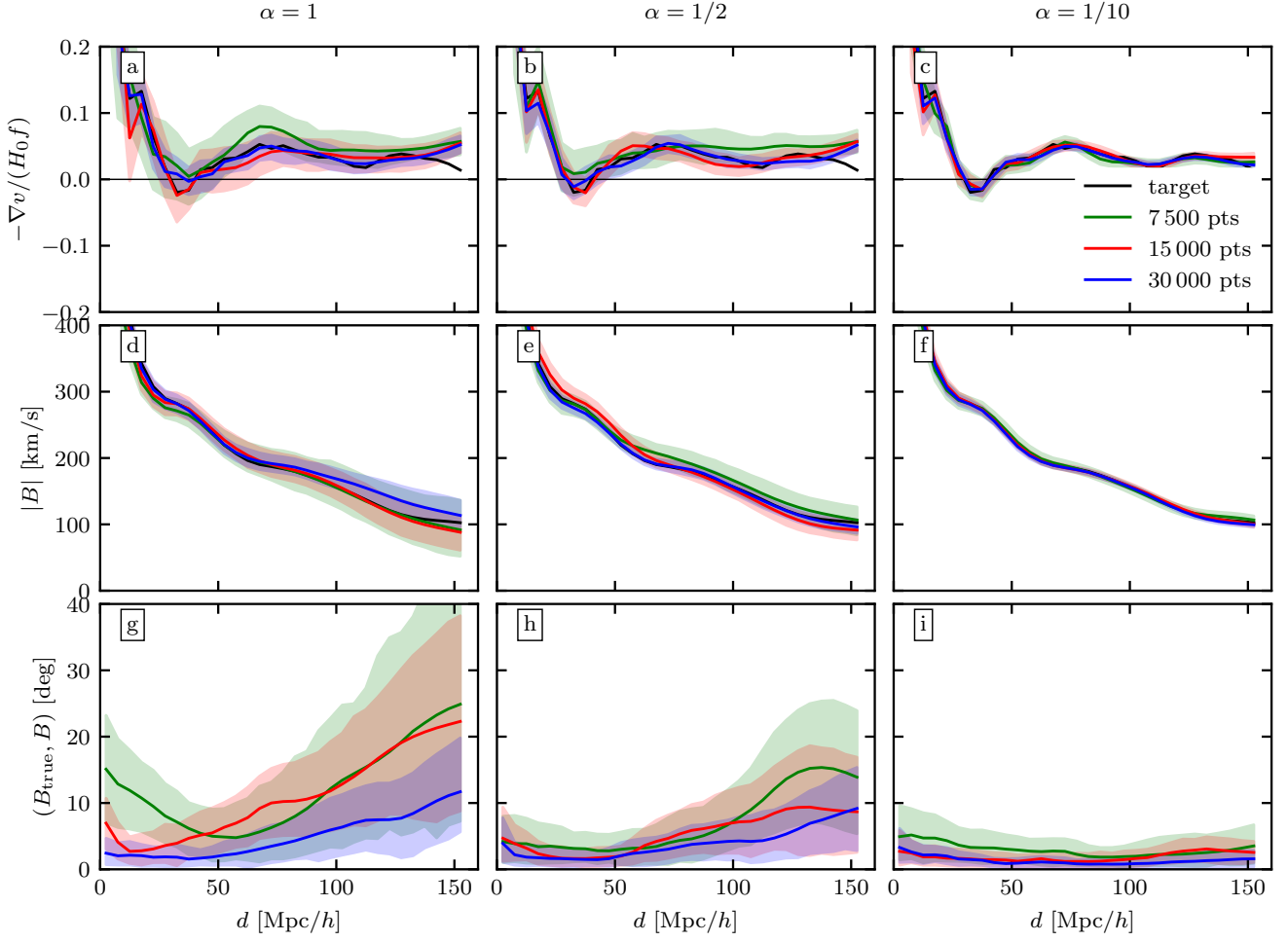


Figure 8. Top row: The monopole moment (namely the mean fractional over-density; upper panel), the amplitude (middle panel) and alignment (with the target; lower panel) of the dipole moment (namely the bulk velocity) are shown for $\alpha = 1, 1/2$ and $1/10$ (columns left to right) and for $N = (0.75, 1.5, 3.0) \times 10^4$, where N is the number of data points. The mean (solid lines) and the scatter are calculated over the ensemble of HMC steps. The moments of the target field are shown in black.

[Society](#), 498, 2968

Lynden-Bell D., Faber S. M., Burstein D., Davies R. L., Dressler A., Terlevich R. J., Wegner G., 1988, *ApJ*, **326**, 19

Neal R., 2011, in , *Handbook of Markov Chain Monte Carlo*. pp 113–162, [doi:10.1201/b10905](#)

Peebles P. J. E., 1980, *The large-scale structure of the universe*

Sorce J. G., 2015, *MNRAS*, **450**, 2644

Sorce J. G., et al., 2016, *MNRAS*, **455**, 2078

Strauss M. A., Willick J. A., 1995, *Phys. Rep.*, **261**, 271

Tully R. B., Shaya E. J., Karachentsev I. D., Courtois H. M., Kocevski D. D., Rizzi L., Peel A., 2008, *ApJ*, **676**, 184

Tully R. B., et al., 2013, *AJ*, **146**, 86

Tully R. B., Courtois H. M., Sorce J. G., 2016, *AJ*, **152**, 50

Weinberg S., 2008, *Cosmology*

Yepes G., Gottlöber S., Hoffman Y., 2014, *New Astron. Rev.*, **58**, 1

Zaroubi S., Hoffman Y., Fisher K. B., Lahav O., 1995, *ApJ*, **449**, 446

Zaroubi S., Hoffman Y., Dekel A., 1999, *ApJ*, **520**, 413

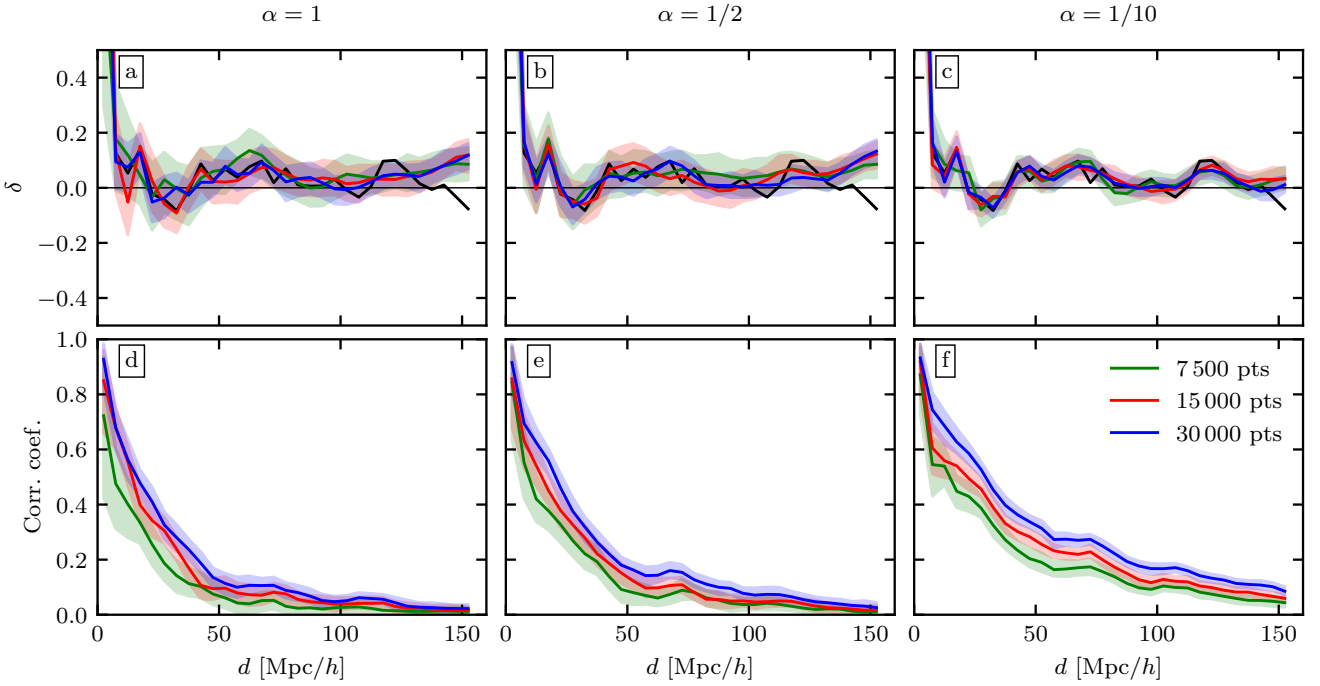


Figure 9. Top row: The mean plus-minus standard deviation of the density field per distance shell is shown for $\alpha = 1, 1/2$ and $1/10$ (left to right). In black we show the target results while in green, red and blue we show the curves reconstructed from 7 500, 15 000 and 30 000 points respectively. Beyond this region there are no constraints. Bottom row: same plots but for the correlation between the reconstructed field and the target field.

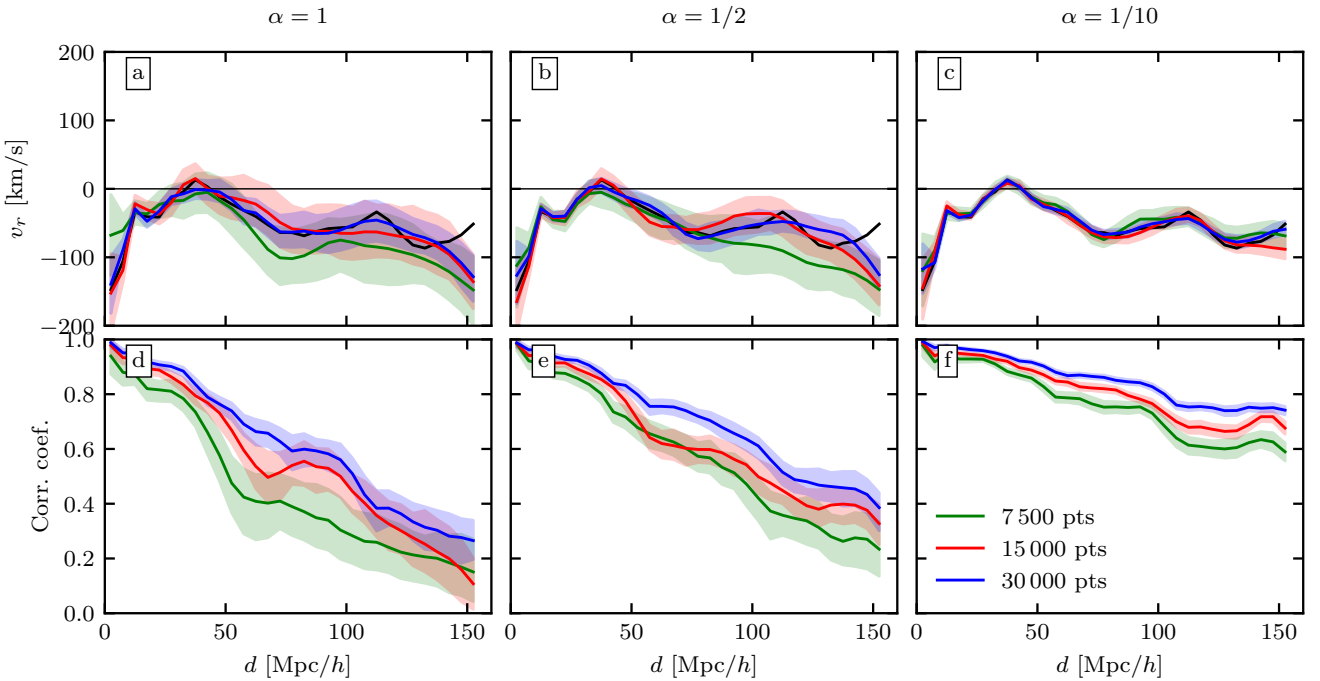


Figure 10. Same as Fig. 9 but for the radial velocity field instead of the density field.